

Frequency-tunable spiking dynamics of Chua corsage memristors

Qijian Wu(吴奇键), Peipei Jin(靳培培), Xiameng Wu(吴夏萌), Meiyuan Gu(顾梅园), Wei Zhou(周玮), Yujiao Dong(董玉姣), Yan Liang(梁燕), and Long Chen(陈龙)
Citation: Chin. Phys. B, 2026, 35 (**4**): 048703. DOI: 10.1088/1674-1056/ae3c95
http://cpb.iphy.ac.cn; http://iopscience.iop.org/cpb

What follows is a list of articles you may be interested in

Bifurcation dynamics govern sharp wave ripple generation and rhythmic transitions in hippocampal-cortical memory networks

Xin Jiang(姜鑫), Jialiang Nie(聂嘉良), Denggui Fan(樊登贵), and Lixia Duan(段利霞)
Chin. Phys. B, 2025, 34 (**12**): 128702. DOI: 10.1088/1674-1056/ae111d

Coexisting fast-slow dendritic traveling waves in a 3D-array electric field coupled neuronal network

Xile Wei(魏熙乐), Zeyu Ren(任泽宇), Meili Lu(卢梅丽), Yaqin Fan(樊亚琴), and Siyuan Chang(常思远)
Chin. Phys. B, 2024, 33 (**6**): 068702. DOI: 10.1088/1674-1056/ad3228

Synchronization and firing mode transition of two neurons in a bilateral auditory system driven by a high-low frequency signal

Charles Omotomide Apata, Yi-Rui Tang(唐浥瑞), Yi-Fan Zhou(周祎凡), Long Jiang(蒋龙), and Qi-Ming Pei(裴启明)
Chin. Phys. B, 2024, 33 (**5**): 058704. DOI: 10.1088/1674-1056/ad1a8e

Dynamical behaviors in discrete memristor-coupled small-world neuronal networks

Jieyu Lu(鲁婕妤), Xiaohua Xie(谢小华), Yaping Lu(卢亚平), Yalian Wu(吴亚联), Chunlai Li(李春来), and Minglin Ma(马铭磷)
Chin. Phys. B, 2024, 33 (**4**): 048701. DOI: 10.1088/1674-1056/ad1483

Effect of cognitive training on brain dynamics

Guiyang Lv(吕贵阳), Tianyong Xu(徐天勇), Feiyan Chen(陈飞燕), Ping Zhu(朱萍), Miao Wang(王淼), and Guoguang He(何国光)
Chin. Phys. B, 2024, 33 (**2**): 028704. DOI: 10.1088/1674-1056/ad09c8

SPECIAL TOPIC — Biophysical circuits: Modeling & applications in neuroscience

Frequency-tunable spiking dynamics of Chua corsage memristors

Qijian Wu(吴奇键)[1], Peipei Jin(靳培培)[1,†], Xiameng Wu(吴夏萌)[1], Meiyuan Gu(顾梅园)[1], Wei Zhou(周玮)[2], Yujiao Dong(董玉姣)[1], Yan Liang(梁燕)[1], and Long Chen(陈龙)[1]

[1] *Institute of Modern Circuit and Intelligent Information, Hangzhou Dianzi University, Hangzhou* 310018, *China*
[2] *School of Information Science and Engineering, NingboTech University, Ningbo* 315042, *China*

(Received 17 December 2025; revised manuscript received 22 January 2026; accepted manuscript online 23 January 2026)

Brain-inspired computing relies on neuronal spiking frequency as a foundational element for information encoding. Bi-directional spiking enables the processing and encoding of multimodal information. The Chua corsage memristor (CCM), endowed with the edge of chaos, can generate spiking dynamics and can be synthesized using only off-the-shelf electronic components, making it suitable for both theoretical analysis and hardware demonstration of frequency-tunable spiking dynamics. This paper employs second- and third-order neuron circuits constructed with a CCM sibling, namely the odd-symmetric CCM, to explore the frequency-tunable characteristics of bi-directional spiking. A quantitative method for calculating the output spiking frequency of neurons is proposed. Simulation results verify the validity of this method. The neuron hardware circuits are implemented using a homemade odd-symmetric CCM circuit board. The experimental results confirm the frequency-tunable spiking of the odd-symmetric CCM-based neurons and reveal the effect of the excitation voltage on the system dynamics.

Keywords: Chua corsage memristor, edge of chaos, neuron circuit, frequency-tunable dynamic

PACS: 87.19.ll, 05.45.–a, 82.40.Bj

DOI: 10.1088/1674-1056/ae3c95 **CSTR:** 32038.14.CPB.ae3c95

1. Introduction

With the rapid development of artificial intelligence technologies such as intelligent healthcare, autonomous driving and robotics,[1–3] the demand for processing massive data and executing complex computing tasks has grown dramatically. However, the traditional von Neumann architecture faces increasing bottlenecks in energy efficiency and data transfer.[4] Memristors, which are capable of emulating biological synapses and neurons, possess inherent advantages including low power consumption, high processing speed, and in-memory computing.[5] These attributes make them well suited for neuromorphic computing, artificial neural network implementation, and brain-inspired edge AI applications.[6–9] Consequently, they have attracted significant attention as a promising class of devices for future computing systems.

Locally active memristors serve as key devices for realizing bio-inspired neuronal functions.[10] In contrast to locally passive memristors, locally active devices exhibit a negative differential resistance (NDR) region within a specific voltage range, enabling spontaneous oscillations and spiking discharges.[11] Chua pioneered the use of locally active memristors to construct the first neuron model based on the classical Hodgkin–Huxley model.[12] After that, HRL Laboratories reported neuron circuits based on VO_2 locally active memristors that emulate a large number of biological neuronal behaviors.[13] HP Laboratories fabricated an NbO_2 Mott locally active memristor-based nanocircuit, capable of generating fifteen distinct neuromorphic functionalities.[14] Reference [15] reported a multimodal fused sensory spiking neuron based on an NbO_2 device, which produces spikes to encode multimodal information, such as pressure and temperature via frequency modulation. Chaotic circuits and neurons based on TiO_2 memristors have been presented in Refs. [16,17]. Unlike conventional electronic circuit components, memristor devices such as the NbO_2 Mott memristor and the VO_2 memristor are fabricated using advanced nanofabrication machines. Their fabrication is often time consuming and expensive, which is unaffordable for most researchers and poses challenges for experimental validation of memristive neurons and neural networks.

Chua corsage memristor (CCM), a hypothetical locally active memristor proposed by L. Chua, is endowed with the edge of chaos (EOC), making it possible to generate neuromorphic dynamics.[18] Importantly, a functioning homemade CCM circuit board has been built, facilitating the hardware demonstration of neuromorphic behaviors in Refs. [19,20]. Adding an inductor and a capacitor to the CCM gives rise to a neuron exhibiting many well-known neuromorphic behaviors, thereby verifying the neuromorphic dynamics of the CCM.[18] In addition, three CCM siblings, dubbed the asymmetric CCM, odd-symmetric CCM and the current-controlled CCM, have been presented in Refs. [18,21,22]. The odd-

†Corresponding author. E-mail: jinpeipei@hdu.edu.cn

© 2026 Chinese Physical Society and IOP Publishing Ltd. All rights, including for text and data mining, AI training, and similar technologies, are reserved.

symmetric CCM, featuring two symmetrical NDR regions, exhibits biphasic action potentials that have not been observed so far in memristive circuits.[21] Reference [22] reported the first hardware observation of Turing instability phenomena on two homemade current-controlled CCM circuit boards. In addition, a discrete corsage memristor and its neuromorphic dynamics were investigated in Refs. [23,24].

Second- and third-order neuronal circuits were constructed by combining VO_2 locally active memristors with inductors and capacitors.[25] Discontinuous neuronal models were built by coupling locally active discrete memristors into discrete neurons and synapses.[26] Sodium and potassium ion channels in the Wilson neuron were modeled as locally active and passive memristors, respectively.[27] In addition, a two-dimensional parametric polynomial chaotic system offers a compact nonlinear framework for describing tunable chaos.[28] A multi-valued model enables the generation of complex chaotic and fractal dynamics, providing an effective mechanism for modeling multistable and nonlinear firing behavior.[29] The existing studies have focused on the types of neuromorphic behaviors in memristive neurons, but their frequency characteristics have been largely unexplored.

The spiking frequency of neurons plays a crucial role in information encoding and transmission for brain-inspired computing. A multimode-fused spiking neuron that integrates pressure and temperature sensing into a single memristive neuron was proposed, where multisensory information is fused into one spike train and encoded through spiking frequency modulation.[15] A scalable memristor-based neural circuit generates biologically inspired spiking trains and achieves real-time obstacle avoidance in robotic systems through frequency-coded control with remarkably low latency.[30] An ion–electron hybrid memristive neuron is capable of wide-range frequency tuning, which enables biomotor control via frequency-regulated muscle activation and frequency-coded pattern recognition tasks.[31] These results demonstrate the importance of spiking-frequency modulation for efficient and low-latency edge intelligence in neuromorphic sensing and control systems.

The motivation of this paper is to apply Chua's theories of local activity and edge of chaos to investigate the frequency characteristics of spiking generated by the CCM and to establish a quantitative method for calculating the spiking frequency, thereby enabling the adjustment and control of spiking frequency.

With regard to the organization of this paper, the symmetric local activity and EOC of a CCM sibling are analyzed in Section 2. A second-order neuron is built, and its spiking frequency characteristics are investigated in Section 3. Section 4 presents frequency-tunable spiking in a third-order neuron and proposes a quantitative method to determine the spiking frequency. Experimental verification of the frequency-tunable spiking from a homemade CCM circuit board is presented in Section 5. Section 6 concludes this paper.

2. Chua corsage memristor sibling

Odd-symmetric CCM (OS-CCM), a sibling of the CCM, features the generation of bidirectional action potentials, which is inherently consistent with the bipolar operating characteristics of practical CMOS analog circuits. Given that bidirectional action potentials are applicable to brain-inspired multimodal recognition, this paper investigates their frequency characteristics using the OS-CCM, thereby providing crucial theoretical support for multimodal recognition and computing. Moreover, a functioning homemade circuit board of the OS-CCM has been built using only off-the-shelf electronic components,[21] facilitating the hardware verification of the frequency characteristics of bidirectional action potentials.

The equations of the OS-CCM are defined as follows and have been presented in our previous work[21]

$$i_{\mathrm{M}} = G(x)v_{\mathrm{M}} = G_0 x^2 v_{\mathrm{M}}, \tag{1}$$

$$\frac{\mathrm{d}x}{\mathrm{d}t} = g(x, v_{\mathrm{M}}) = K(30 - x + |x-14| - |x-46| + v_{\mathrm{M}}^2), \tag{2}$$

where i_{M}, v_{M}, and x represent the current, voltage, and state variable of the OS-CCM, respectively; $G_0 = 10^{-2}$ and $K = 10^4$ are scaling constants chosen to ensure both theoretical stability and practical circuit realizability; $G(x) = G_0 x^2$ denotes the memductance function of the OS-CCM. The squared voltage term in Eq. (2) gives rise to the odd-symmetric DC V–I characteristics and the generation of bidirectional action potentials in the OS-CCM.

2.1. Odd-symmetric DC V–I curve

The DC V–I curve and its enlarged negative differential resistance (NDR) domains of the OS-CCM are plotted in Fig. 1, derived by setting $\mathrm{d}x/\mathrm{d}t = 0$ and solving Eqs. (1) and (2) with $x = X$, $i_{\mathrm{M}} = I_{\mathrm{M}}$, and $v_{\mathrm{M}} = V_{\mathrm{M}}$.

Figure 1(b) shows the three-branch DC V–I curve of the OS-CCM over the range $-2 < X < 14$. It is odd-symmetric, which is why this memristor is referred to as an odd-symmetric CCM. The blue branch in the DC V–I curve of the OS-CCM contains two NDR sub-domains marked by two dark-blue dashed boxes, whose enlarged views are shown in Figs. 1(a) and 1(c). Figure 1(a) shows an N-shaped sub-branch that includes the first NDR sub-domain (NDR1) over the voltage range $-1.413\ \mathrm{V} < V_{\mathrm{M}} < -0.629\ \mathrm{V}$ and $-16\ \mathrm{mA} < I_{\mathrm{M}} < 0\ \mathrm{mA}$. Figure 1(c) shows the second NDR sub-domain (NDR2) over the voltage range $0.629\ \mathrm{V} < V_{\mathrm{M}} < 1.413\ \mathrm{V}$ and $0\ \mathrm{mA} < I_{\mathrm{M}} < 16\ \mathrm{mA}$. Importantly, the NDR domain is a fingerprint of local activity, which enables the memristor to generate action potentials.

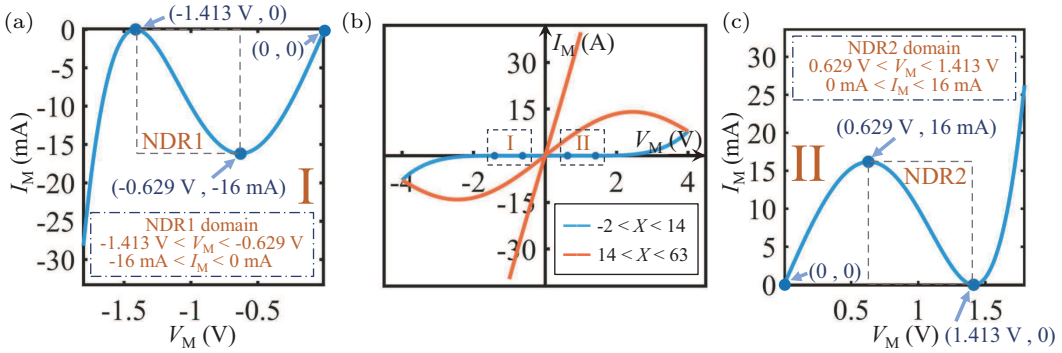


Fig. 1. (a) Enlarged view of the left blue N-shaped branch I, showing the first NDR sub-branch over the ranges $-1.413\ \text{V} < V_\text{M} < -0.629\ \text{V}$ and $-16\ \text{mA} < I_\text{M} < 0\ \text{mA}$. (b) Odd-symmetric DC V–I curve of the OS-CCM obtained over the range $-2 < X < 63$, which contains two negative-slope domains in its blue branch. (c) Enlarged view of the right blue N-shaped branch II, showing the second NDR sub-branch over the ranges $0.629\ \text{V} < V_\text{M} < 1.413\ \text{V}$ and $0\ \text{mA} < I_\text{M} < 16\ \text{mA}$.

2.2. Local activity and edge of chaos (EOC)

EOC, a stable subset of the locally active domain (LAD), is essential for the generation of action potentials. To locate the voltage range where bidirectional action potentials occur, Chua's local activity theorem and EOC criterion are applied to calculate the LAD and edge of chaos domain (EOCD) of the OS-CCM.

Here, the method for identifying the EOCD of memristive circuits is briefly reviewed. A voltage-controlled memristive circuit is on the EOC if and only if its small-signal admittance $Y(s,Q)$ satisfies both of the following conditions:[32]

(i) the frequency response satisfies $\text{Re}[Y(\text{i}\omega,Q)] < 0$ for some $-\infty < \omega < \infty$;

(ii) all poles s_p of $Y(s,Q)$ are in the open left half plane (LHP), where $\text{Re}[s_\text{p}] < 0$.

Note that the NDR domains, which are capable of amplifying small signals, of the OS-CCM are observed on the blue branch with $X < 14$ of its DC V–I characteristic in Figs. 1(a) and 1(c). For $X < 14$, the relationships among the voltage V_M, the current I_M, and the state variable X, derived by setting $\text{d}x/\text{d}t = g(X,V_\text{M}) = 0$ in Eq. (2), are given as follows:

$$X = V_\text{M}^2 - 2, \tag{3}$$

$$I_\text{M} = G_0 X^2 V_\text{M}. \tag{4}$$

The admittance function of the CCM at the equilibrium point has been derived in our previous work.[18] Following the same procedure, the admittance function $Y(s,Q)$ of the OS-CCM at the equilibrium point Q is obtained as

$$Y(s,Q) = \frac{4KG_0XV_\text{M}^2 + KG_0X^2 + sG_0X^2}{s+K}. \tag{5}$$

It can be seen that $Y(s,Q)$ exhibits a pole $s_\text{p} = -K = -10^4 < 0$, which implies the asymptotic stability of the OS-CCM over the range $X < 14$ on the blue branch of its DC V–I curve.

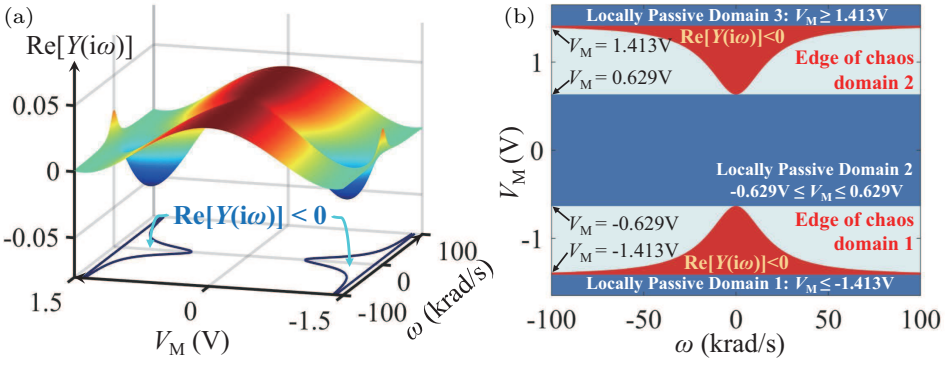


Fig. 2. (a) The landscape of $\text{Re}[Y(\text{i}\omega,Q)]$ over the ranges $-100\ \text{krad/s} < \omega < 100\ \text{krad/s}$ and $-1.5\ \text{V} < V_\text{M} < 1.5\ \text{V}$. The bottom dark-blue curve, mapped onto the ω vs. V_M plane, is the projection of $\text{Re}[Y(\text{i}\omega,Q)] = 0$. (b) Parameter map of the OS-CCM in the ω vs. V_M plane, where the red region corresponds to $\text{Re}[Y(\text{i}\omega,Q)] < 0$, representing the EOCD over the ranges $-1.413\ \text{V} < V_\text{M} < -0.629\ \text{V}$ and $0.629\ \text{V} < V_\text{M} < 1.413\ \text{V}$.

By substituting $s = \text{i}\omega$ into Eq. (5) to obtain its frequency response and extracting the real part, $\text{Re}[Y(\text{i}\omega,Q)]$ can be derived as follows:

$$\text{Re}[Y(\text{i}\omega,Q)] = \frac{4K^2G_0XV_\text{M}^2 + K^2G_0X^2 + G_0X^2\omega^2}{K^2+\omega^2}. \tag{6}$$

Thereafter, the 3D distribution of $\text{Re}[Y(\text{i}\omega,Q)]$ as a function of ω and V_M is plotted in Fig. 2(a). The contour where $\text{Re}[Y(\text{i}\omega,Q)] = 0$ delineates the locally active parameter range, as shown in Fig. 2(b).

Figure 2(a) shows the landscape of $\text{Re}[Y(\text{i}\omega,Q)]$, where

the dark-blue contour at the bottom represents the projection of $\mathrm{Re}[Y(\mathrm{i}\omega,Q)]=0$. Inside the dark-blue contour, $\mathrm{Re}[Y(\mathrm{i}\omega,Q)]<0$. Figure 2(b) shows the parameter map of the OS-CCM, where the red color denotes the region of $\mathrm{Re}[Y(\mathrm{i}\omega,Q)]<0$. According to condition (i) of Chua's EOC criterion, the existence of $\mathrm{Re}[Y(\mathrm{i}\omega,Q)]<0$ indicates the local activity of the OS-CCM for some ω over the ranges $-1.413\ \mathrm{V}<V_\mathrm{M}<-0.629\ \mathrm{V}$ and $0.629\ \mathrm{V}<V_\mathrm{M}<1.413\ \mathrm{V}$. The negative pole $s=-K=-10^4$ derived from Eq. (5) indicates its asymptotic stability, satisfying condition (ii) of Chua's EOC criterion. Hence, the OS-CCM operates in the EOCD over the ranges $-1.413\ \mathrm{V}<V_\mathrm{M}<-0.629\ \mathrm{V}$ and $0.629\ \mathrm{V}<V_\mathrm{M}<1.413\ \mathrm{V}$ with $X<14$, which matches the intersection of the red and gray regions shown in Fig. 2(b). The blue region corresponds to the locally passive domain (LPD), within which no periodic spiking occurs. Figures 2(a) and 2(b) are symmetric with respect to the voltage axis $V=0$.

This section presents the odd-symmetric characteristics of the OS-CCM and demonstrates its LAD and EOCD by applying Chua's criterion, thereby providing the theoretical foundation for exploring the frequency characteristics of OS-CCM-based neuromorphic dynamics.

3. Second-order neuron and its frequency-tunable spiking

The previous section has demonstrated the local activity and EOC of the OS-CCM, which can be destabilized to generate periodic spiking. Since the original CCM exhibits capacitive behavior in its EOCD, an external inductor is required to form a second-order neuron circuit.[18] The inductance value can be determined by the impedance compensation method.[33] To analyze the reactance characteristics of the OS-CCM, its frequency response curves $\mathrm{Re}[Y(\mathrm{i}\omega,Q_1)]$ and $\mathrm{Im}[Y(\mathrm{i}\omega,Q_1)]$ are plotted at an equilibrium point $Q_1(X,V_\mathrm{M})=(-1.320,0.825\ \mathrm{V})$ within its LAD and EOCD in Fig. 3(a). The second-order neuron based on the OS-CCM and its small-signal equivalent circuit are illustrated in Fig. 3(b).

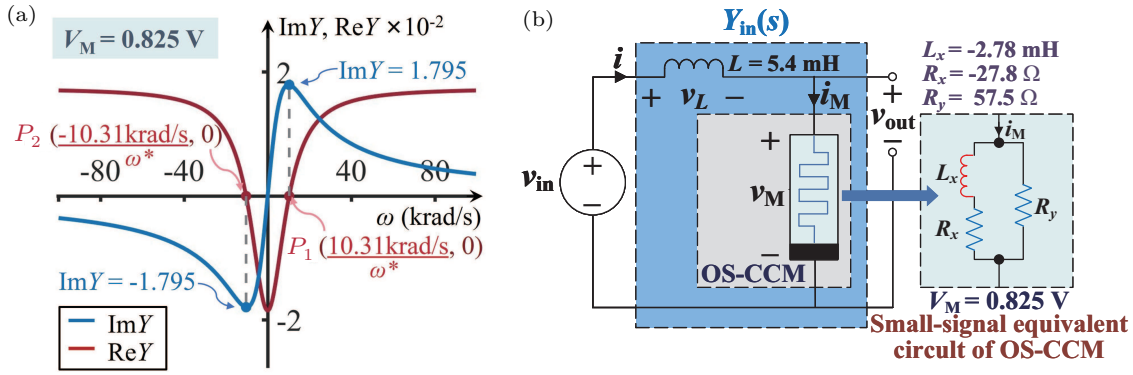


Fig. 3. (a) Frequency response of $\mathrm{Re}[Y(\mathrm{i}\omega)]$ and $\mathrm{Im}[Y(\mathrm{i}\omega)]$ over the range $-100\ \mathrm{krad/s}<\omega<100\ \mathrm{krad/s}$ at the equilibrium point Q_1 with $V_\mathrm{M}=0.825$ V. (b) OS-CCM-based second-order neuron constructed with an OS-CCM and an inductor, whose small-signal equivalent circuit on the right consists of R_x, L_x, and R_y in series and parallel connection at Q_1.

Figure 3(a) shows the frequency response of $\mathrm{Re}[Y(\mathrm{i}\omega,Q_1)]$ and $\mathrm{Im}[Y(\mathrm{i}\omega,Q_1)]$ over the range $-100\ \mathrm{krad/s}<\omega<100\ \mathrm{krad/s}$. From Fig. 3(a), the curve $\mathrm{Re}[Y(\mathrm{i}\omega,Q_1)]$ intersects the ω-axis at two points P_1 (10.31 krad/s, 0) and P_2 (–10.31 krad/s, 0), indicating that at $\omega^*=\pm10.31$ krad/s, one obtains $\mathrm{Re}[Y(\mathrm{i}\omega^*,Q_1)]=0$. Also, at $\omega^*=10.31$ krad/s, $\mathrm{Im}[Y(\mathrm{i}\omega^*,Q_1)]=1.795\times10^{-2}$, implying that the OS-CCM exhibits capacitive characteristics. According to the compensation method in Ref. [33], the external inductance value can be obtained from $L=1/(\omega^*\mathrm{Im}[Y(\mathrm{i}\omega^*,Q_1)])=1/(10.31\times0.01795)=5.4$ mH.

Figure 3(b) shows the second-order neuron constructed with an OS-CCM and an inductor. The inset on the right side illustrates the small-signal equivalent circuit of the OS-CCM at the equilibrium point Q_1, which includes three components: a negative inductor $L_x=-2.78\ \mathrm{mH}<0$, a negative resistor $R_x=-27.8\ \Omega<0$, and a positive resistor $R_y=57.5\ \Omega>0$. The small-signal equivalent circuit of the OS-CCM further reveals its negative inductance characteristic, i.e., capacitive behavior. Based on the principle of LC oscillation, the neuron in Fig. 3(b) is capable of generating oscillations.

3.1. Edge of chaos

To analyze the impact of the external inductor on the EOCD of the OS-CCM, one needs to calculate the EOCD of the second-order neuron circuit. The admittance function $Y_\mathrm{in}(s,Q')$ at the equilibrium point $Q'=(X,I_L=I_\mathrm{M}=G_0X^2V_\mathrm{M})$ of the second-order neuron in Fig. 3(b) is as follows:

$$Y_\mathrm{in}(s,Q')=\frac{Y_LY}{Y_L+Y}=\frac{G_0X^2s+4KG_0XV^2+KG_0X^2}{G_0X^2Ls^2+(4KG_0XV^2L+KG_0X^2L+1)s+K}. \quad (7)$$

The admittance function of the external inductance is $Y_L=1/(sL)$. At the DC limit ($s=0$), $Y_L\to\infty$, and the inductor in the neuron circuit can be considered a short circuit. Hence, the DC operating point of the input voltage V_in coincides with that of the OS-CCM, i.e., $V_\mathrm{in}=V_\mathrm{M}=V$.

By substituting $s = \mathrm{i}\omega$ into Eq. (7) to yield the frequency response of the admittance function of the second-order neuron and extracting its real part, one obtains $\mathrm{Re}[Y_{\mathrm{in}}(\mathrm{i}\omega, Q')]$ as follows:

$$\mathrm{Re}[Y_{\mathrm{in}}(\mathrm{i}\omega, Q')] = \frac{G_0X^2\omega^2 + K^2G_0X^2 + 4K^2G_0XV^2}{(K - G_0X^2L\omega^2)^2 + (1 + KG_0X^2L + 4KG_0XV^2L)^2\omega^2}. \tag{8}$$

The two poles can be obtained by solving the denominator of Eq. (7), as given by

$$s_{\mathrm{p1}} = \frac{-(4KG_0XV^2L + KG_0X^2L + 1) - \sqrt{(4KG_0XV^2L + KG_0X^2L + 1)^2 - 4KG_0X^2L}}{2G_0X^2L}, \tag{9}$$

$$s_{\mathrm{p2}} = \frac{-(4KG_0XV^2L + KG_0X^2L + 1) + \sqrt{(4KG_0XV^2L + KG_0X^2L + 1)^2 - 4KG_0X^2L}}{2G_0X^2L}. \tag{10}$$

To determine the EOCD of the second-order neuron, the 3D distributions of $\mathrm{Re}[Y_{\mathrm{in}}(\mathrm{i}\omega)]$, $\mathrm{Re}[s_{\mathrm{p1}}]$ and $\mathrm{Re}[s_{\mathrm{p2}}]$ as a function of ω and V are plotted in Figs. 4(a)–4(c). The projected curves defined by $\mathrm{Re}[Y_{\mathrm{in}}(\mathrm{i}\omega)] = 0$, $\mathrm{Re}[s_{\mathrm{p1}}] = 0$, and $\mathrm{Re}[s_{\mathrm{p2}}] = 0$ collectively delineate the parameter map of the neuron circuit, as shown in Fig. 4(d).

Figure 4(a) shows the 3D surface plot depicting $\mathrm{Re}[Y_{\mathrm{in}}(\mathrm{i}\omega)]$ in the ω vs. V plane, where the sky-blue contour at the bottom is the projection of $\mathrm{Re}[Y_{\mathrm{in}}(\mathrm{i}\omega)] = 0$, corresponding to the red region, marked $\mathrm{Re}[Y_{\mathrm{in}}(\mathrm{i}\omega)] < 0$, in Fig. 4(d).

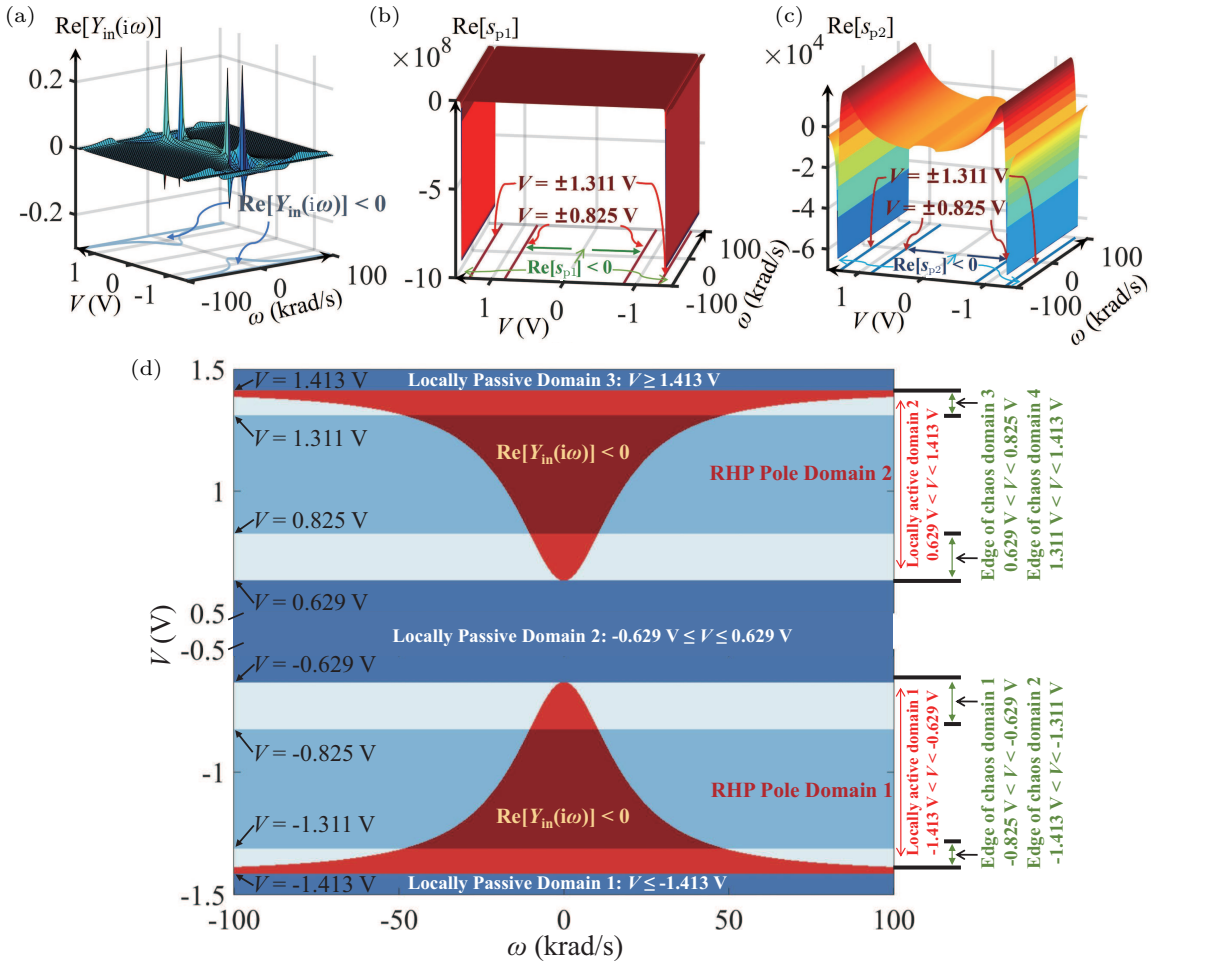


Fig. 4. (a) 3D surface plot of $\mathrm{Re}[Y_{\mathrm{in}}(\mathrm{i}\omega)]$ over the ranges -100 krad/s $< \omega <$ 100 krad/s and -1.5 V $< V <$ 1.5 V. The bottom sky-blue curve on the ω vs. V plane is the projection of $\mathrm{Re}[Y_{\mathrm{in}}(\mathrm{i}\omega)] = 0$. Also shown are 3D surface plots of $\mathrm{Re}[s_{\mathrm{p1}}]$ in (b) and $\mathrm{Re}[s_{\mathrm{p2}}]$ in (c) over the same frequency and voltage ranges. The projected lines at the bottom denote $\mathrm{Re}[s_{\mathrm{p1}}] = 0$ and $\mathrm{Re}[s_{\mathrm{p2}}] = 0$, which separate the stable region ($\mathrm{Re}[s_{\mathrm{p1,2}}] < 0$) and the unstable region ($\mathrm{Re}[s_{\mathrm{p1}}] > 0$ or $\mathrm{Re}[s_{\mathrm{p2}}] > 0$). (d) Parameter map of the second-order neuron in the ω vs. V plane. The projected curves from panels (a) to (c) clearly separate the LAD, LPD, and EOCD. The intersection of the red and gray regions corresponds to the EOCD over the voltage ranges -1.413 V $< V < -1.311$ V, -0.825 V $< V < -0.629$ V, 0.629 V $< V <$ 0.825 V, and 1.311 V $< V <$ 1.413 V. The intersection of the light-blue and dark-red regions indicates the RHP pole domain over the voltage ranges -1.311 V $< V < -0.825$ V and 0.825 V $< V <$ 1.311 V.

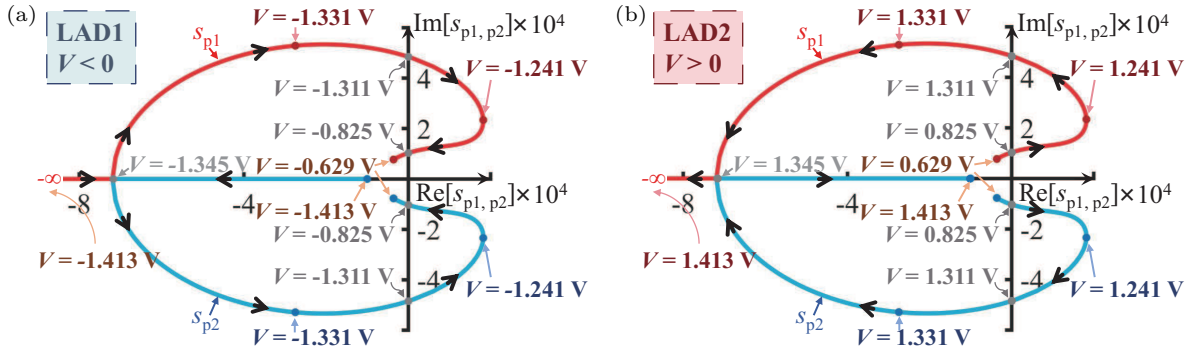


Fig. 5. Migration trajectories of the poles of the second-order neuron with $L = 5.4$ mH in the LAD1 over the voltage range $-1.413\ \text{V} < V < -0.629\ \text{V}$ in panel (a) and in the LAD2 over the voltage range $0.629\ \text{V} < V < 1.413\ \text{V}$ in panel (b).

Figures 4(b) and 4(c) show the 3D surface plots depicting $\text{Re}[s_{\text{p1}}]$ and $\text{Re}[s_{\text{p2}}]$. Similarly, the bottom red and blue lines on the ω vs. V plane mark the projections of $\text{Re}[s_{\text{p1}}] = 0$ and $\text{Re}[s_{\text{p2}}] = 0$, respectively. Figure 4(a) indicates the neuron is locally active over the ranges $-1.413\ \text{V} < V < -0.629\ \text{V}$ and $0.629\ \text{V} < V < 1.413\ \text{V}$ with $\text{Re}[Y_{\text{in}}(\text{i}\omega)] < 0$ for some ω (condition (i) of Chua's EOC criterion). Figures 4(b) and 4(c) demonstrate that the neuron is stable over the voltage ranges $V < -1.311\ \text{V}$, $-0.825\ \text{V} < V < 0.825\ \text{V}$ and $V > 1.311\ \text{V}$ with $\text{Re}[s_{\text{p1}}] < 0$ and $\text{Re}[s_{\text{p2}}] < 0$. Figure 4(d) shows a parameter map of the second-order neuron in the ω vs. V plane, where the intersection of the red and gray regions is the EOCD (locally active and stable) over the voltage ranges $-1.413\ \text{V} < V < -1.311\ \text{V}$, $-0.825\ \text{V} < V < -0.629\ \text{V}$, $0.629\ \text{V} < V < 0.825\ \text{V}$ and $1.311\ \text{V} < V < 1.413\ \text{V}$. The intersection of the dark-red and light-blue regions represents the RHP pole domain (locally active and unstable), in which action potentials can be observed, over the voltage ranges $-1.311\ \text{V} < V < -0.825\ \text{V}$ and $0.825\ \text{V} < V < 1.311\ \text{V}$.

Furthermore, the migration trajectories of the poles s_{p1} and s_{p2}, defined by Eqs. (9) and (10), in the two LADs of the neuron over the ranges $-1.413\ \text{V} < V < -0.629\ \text{V}$ and $0.629\ \text{V} < V < 1.413\ \text{V}$ are plotted in Fig. 5 to explore the oscillation mechanism of the action potentials.

Figure 5 depicts the migration trajectories of the poles of the second-order neuron in its two symmetric LADs: LAD1 over the ranges $-1.413\ \text{V} < V < -0.629\ \text{V}$ (Fig. 5(a)) and LAD2 over $0.629\ \text{V} < V < 1.413\ \text{V}$ (Fig. 5(b)), where the black arrows indicate the directions of the poles $s_{\text{p1,2}}$ as the voltage V increases. The trajectories of the poles $s_{\text{p1,2}}$ in Figs. 5(a) and 5(b) share identical curves but exhibit opposite directions of motion. From Fig. 5(a), the poles originate from $s_{\text{p1}} = -\infty$ and $s_{\text{p2}} = -10026$ at $V = -1.413\ \text{V}$, merge at $V = -1.345\ \text{V}$ and then separate along the real axis to form a pair of complex conjugate poles as the voltage V increases. Afterwards, the two poles $s_{\text{p1,2}}$ approach the imaginary axis, subsequently reaching the first Hopf bifurcation point at $V = -1.311\ \text{V}$. As the voltage V continues to increase, the poles enter the right half plane, where the neuron becomes unstable and is capable of generating oscillations, revealing the mechanism of the action potentials. Eventually, the poles return to the left half plane from the second Hopf bifurcation point at $V = -0.825\ \text{V}$ and terminate at $V = -0.629\ \text{V}$.

Compared with Fig. 5(a), Fig. 5(b) shows the migration of the poles $s_{\text{p1,2}}$ moving in the opposite direction in LAD2 over the range $0.629\ \text{V} < V < 1.413\ \text{V}$. Overall, Fig. 5 illustrates the destabilization of the neuron within its two symmetric LADs as a function of the input voltage $v_{\text{in}} = V$, demonstrating its capability to generate bidirectional spiking in both positive and negative input voltages.

3.2. Frequency-tunable spiking

The state equations of the second-order neuron in Fig. 3(b) are given as follows:

$$\begin{aligned}\frac{\text{d}x}{\text{d}t} &= K\left(30 - x + |x-14| - |x-46| + \left(\frac{i_L}{G_0 x^2}\right)^2\right),\\ \frac{\text{d}i_L}{\text{d}t} &= \frac{1}{L}\left(v_{\text{in}} - \frac{i_L}{G_0 x^2}\right),\end{aligned} \tag{11}$$

where x, i_L and v_{in} denote the state variable of the OS-CCM, the current through the inductor, and the input voltage of the neuron, respectively. The output voltage v_{out} is defined by $v_{\text{out}} = v_{\text{M}} = i_L/(G_0 x^2)$.

According to Eq. (11), the output voltage $v_{\text{out}}(t)$ of the neuron can be derived, whose time-domain waveforms under different input voltages are shown in Fig. 6.

Figure 6 shows the output voltage waveforms $v_{\text{out}}(t)$ of the second-order neuron in Fig. 3(b) under different input voltages v_{in}. The upper subplots depict the applied positive (yellow) and negative (green) input voltages v_{in}, while the lower subplots present the corresponding output responses. As $v_{\text{in}} = 0.837\ \text{V}$, the neuron generates a periodic spiking in the upward direction with the frequency $\omega = 9.63\ \text{krad/s}$, indicated by the two red dotted lines, as shown in Fig. 6(a). For the negative input voltage $v_{\text{in}} = -0.837\ \text{V}$, the neuron produces an inverted periodic spiking at the same frequency. As

the input voltage $v_{\rm in}$ increases, the neuron produces sustained periodic spiking, while its frequency monotonically increases, exhibiting a positive dependence of the frequency on the voltage amplitude, as shown in Figs. 6(b)–6(f).

Figure 6 demonstrates that an increase in the strength of the input voltage $v_{\rm in}$ leads to a higher frequency ω of the output periodic spiking, indicating that the OS-CCM-based second-order neuron has frequency-tunable spiking dynamics. Note that as x approaches zero, $v_{\rm out}$ increases excessively, leading to numerical overflow. To prevent that, a small perturbation 25×10^{-6} was added in x^2 to obtain the simulation results in Fig. 6 via MATLAB. For clarity, the input voltages shown in Fig. 6 are rounded to three decimal places.

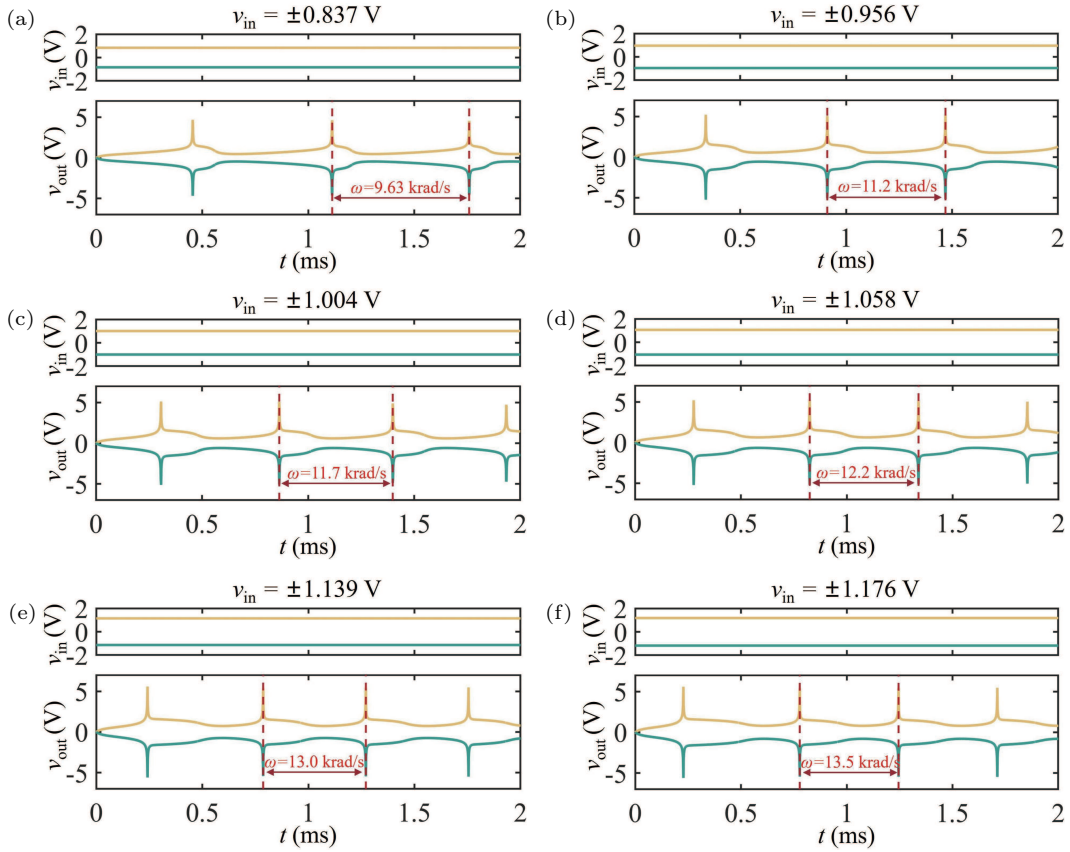


Fig. 6. Time-domain waveforms of the output voltage $v_{\rm out}(t)$ of the second-order neuron under different input voltages and corresponding spiking frequencies: $v_{\rm in} = \pm 0.837$ V in panel (a), $v_{\rm in} = \pm 0.956$ V in panel (b), $v_{\rm in} = \pm 1.004$ V in panel (c), $v_{\rm in} = \pm 1.058$ V in panel (d), $v_{\rm in} = \pm 1.139$ V in panel (e), and $v_{\rm in} = \pm 1.176$ V in panel (f). The yellow periodic spiking in the upward direction corresponds to a positive input voltage, while the green periodic spiking in the downward direction corresponds to a negative input voltage.

3.3. Quantitative analysis of frequency characteristics

To quantitatively analyze the frequency characteristics of the output spiking, the trajectories of the measured spiking frequency ω and the imaginary parts of the poles $\mathrm{Im}[s_{\rm p1,2}]$ under different input voltages $v_{\rm in} = V$ are plotted in Fig. 7.

Figure 7 shows the measured spiking frequency ω in black, and the imaginary part of the poles $\mathrm{Im}[s_{\rm p1,2}]$ in green for negative input voltages over the range $-1.100\ \mathrm{V} < V < -0.825\ \mathrm{V}$ and in red for positive input voltages over $0.825\ \mathrm{V} < V < 1.100\ \mathrm{V}$ (note that $\mathrm{Im}[s_{\rm p2}] = -\mathrm{Im}[s_{\rm p1}]$ over the voltage

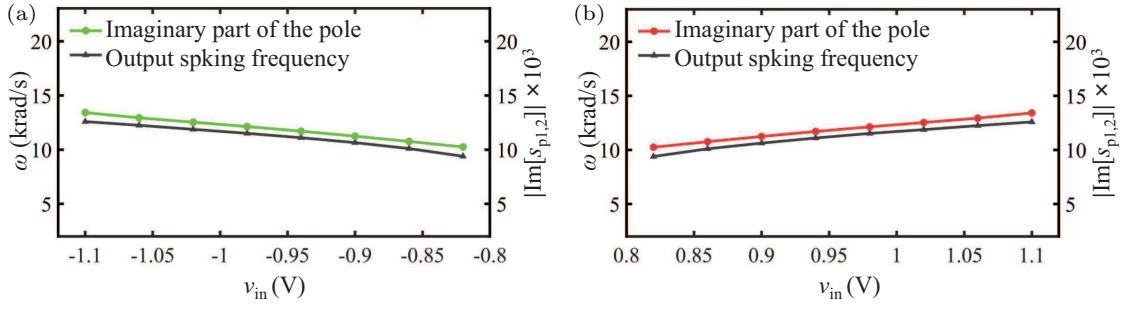


Fig. 7. Trajectories of the measured output spiking frequency ω of the second-order neuron in Fig. 3(b) and the imaginary parts of its poles $\mathrm{Im}[s_{\rm p1,2}]$ over the voltage ranges $-1.100\ \mathrm{V} < V < -0.825\ \mathrm{V}$ in panel (a) and $0.825\ \mathrm{V} < V < 1.100\ \mathrm{V}$ in panel (b).

range). The results indicate that the measured frequency ω closely matches $|\mathrm{Im}[s_{\mathrm{p1,2}}]|$ with a mean error of less than 6%, establishing the approximate relation $\omega \approx |\mathrm{Im}[s_{\mathrm{p1,2}}]|$ over $0.825\ \mathrm{V} < V < 1.100\ \mathrm{V}$. This demonstrates that the neuronal output frequency is precisely controllable and highly predictable, providing a theoretical foundation for brain-inspired computing.

This section thus reveals the output-frequency tuning capability of the OS-CCM-based second-order neuron and establishes that the pole locations can reliably predict the output spiking frequency.

4. Third-order neuron and its frequency-tunable spiking

To observe richer neural waveforms, a capacitor is added to the second-order neuron to form the resulting third-order neuron, as illustrated in Fig. 8.

Figure 8 shows the third-order neuron circuit implemented using an OS-CCM, an inductor ($L = 5.4$ mH), and a capacitor ($C = 10$ nF). The additional capacitor increases the order of the circuit, endowing it with the potential for richer dynamic behavior.

The state equations of the third-order neuron in Fig. 8 are given as follows:

$$\begin{aligned}\frac{\mathrm{d}x}{\mathrm{d}t} &= K(30 - x + |x-14| - |x-46| + v_{\mathrm{C}}^2),\\ \frac{\mathrm{d}i_L}{\mathrm{d}t} &= \frac{1}{L}(v_{\mathrm{in}} - v_{\mathrm{C}}),\\ \frac{\mathrm{d}v_{\mathrm{C}}}{\mathrm{d}t} &= \frac{1}{C}(i_L - G_0 x^2 v_{\mathrm{C}}),\end{aligned} \tag{12}$$

where x, i_L, v_{C}, and v_{in} represent the state variable of the OS-CCM, the current through the inductor, the voltage of the capacitor, and the input voltage of the neuron, respectively. The output voltage v_{out} is defined as $v_{\mathrm{out}} = v_{\mathrm{M}} = v_{\mathrm{C}}$.

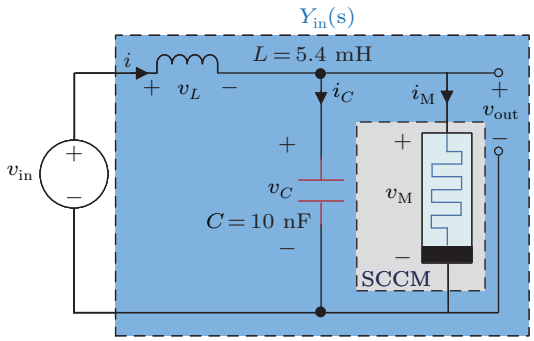


Fig. 8. OS-CCM-based third-order neuron circuit constructed with an OS-CCM, an inductor, and a capacitor.

4.1. Edge of chaos

To examine how the external capacitor affects the EOCD of the second-order neuron in Fig. 3(b), it is necessary to calculate the EOCD of the third-order neuron in Fig. 8. The admittance function $Y_{\mathrm{in}}(s, Q^*)$ at the equilibrium point $Q^* = (X, I_L, V_{\mathrm{C}} = V_{\mathrm{M}})$ of the third-order neuron in Fig. 8 is formulated as

$$Y_{\mathrm{in}}(s,Q^*) = \frac{Cs^2 + (G_0X^2 + KC)s + 4KG_0XV^2 + KG_0X^2}{LCs^3 + (KLC + G_0X^2L)s^2 + (4KG_0XV^2L + KG_0X^2L + 1)s + K}. \tag{13}$$

The frequency response of the admittance function of the third-order neuron is obtained by setting $s = \mathrm{i}\omega$ in Eq. (13), and its real part $\mathrm{Re}[Y_{\mathrm{in}}(\mathrm{i}\omega, Q^*)]$ can be expressed as

$$\mathrm{Re}[Y_{\mathrm{in}}(\mathrm{i}\omega,Q^*)] = \frac{G_0X^2\omega^2 + 4K^2G_0XV^2 + K^2G_0X^2}{[K - L\omega^2(KC + G_0X^2)]^2 + \omega^2[1 + KG_0XL(4V^2 + X) - LC\omega^2]^2}. \tag{14}$$

The three poles of $Y_{\mathrm{in}}(s, Q^*)$ are computed from Eq. (13), and their algebraic expressions are shown as

$$s_{\mathrm{p}i} = -\frac{1}{3}\left(K + \frac{G_0X^2}{C}\right) + \gamma_i\sqrt[3]{\frac{q + \sqrt{q^2 - 4p^3}}{2}} + \frac{\sqrt[3]{2}p}{\gamma_i\sqrt[3]{q + \sqrt{q^2 - 4p^3}}}, \quad i = 1,2,3, \tag{15}$$

where the coefficients are defined as

$$\{\gamma_1, \gamma_2, \gamma_3\} = \left\{-\frac{1}{2} + \frac{\sqrt{3}}{2}\mathrm{j},\ -\frac{1}{2} - \frac{\sqrt{3}}{2}\mathrm{j},\ 1\right\}, \tag{16}$$

$$p = \left(K + \frac{G_0X^2}{C}\right)^2 - \frac{12KG_0XV^2 + 3KG_0X^2}{C} - \frac{3}{LC}, \tag{17}$$

$$q = 2\left(K + \frac{G_0X^2}{C}\right)^3 - \left(9K + \frac{G_0X^2}{C}\right)\left(\frac{4KG_0XV^2 + KG_0X^2}{C} + \frac{1}{LC}\right) + \frac{27K}{LC}. \tag{18}$$

To determine the EOCD of the third-order neuron, its 3D distributions of the real part of the admittance function and the three poles $\mathrm{Re}[Y_{\mathrm{in}}(\mathrm{i}\omega)]$, $\mathrm{Re}[s_{\mathrm{p1,2}}]$, and $\mathrm{Re}[s_{\mathrm{p3}}]$ as a function of ω and V are plotted in Figs. 9(a)–9(c). The projected curves defined by $\mathrm{Re}[Y_{\mathrm{in}}(\mathrm{i}\omega)]=0$, $\mathrm{Re}[s_{\mathrm{p1,2}}]=0$, and $\mathrm{Re}[s_{\mathrm{p3}}]=0$, collectively delineate the parameter map of the neuron circuit, as shown in Fig. 9(d).

Figure 9(a) presents the 3D surface of $\mathrm{Re}[Y_{\mathrm{in}}(\mathrm{i}\omega)]$ on the ω vs. V plane. The bottom sky-blue contour shows the locus $\mathrm{Re}[Y_{\mathrm{in}}(\mathrm{i}\omega)]=0$, corresponding to the two symmetrical red regions marked $\mathrm{Re}[Y_{\mathrm{in}}(\mathrm{i}\omega)]<0$ in Fig. 9(d). The result reveals that the neuron exhibits local activity over the ranges $-1.413\ \mathrm{V}<V<-0.629\ \mathrm{V}$ and $0.629\ \mathrm{V}<V<1.413\ \mathrm{V}$ with $\mathrm{Re}[Y_{\mathrm{in}}(\mathrm{i}\omega)]<0$ for some ω, satisfying condition (i) of Chua's EOC criterion. Figures 9(b) and 9(c) present the 3D surfaces of $\mathrm{Re}[s_{\mathrm{p1,2}}]$ and $\mathrm{Re}[s_{\mathrm{p3}}]$ on the ω vs. V plane. Figure 9(b) indicates that the poles $\mathrm{Re}[s_{\mathrm{p1}}]$ and $\mathrm{Re}[s_{\mathrm{p2}}]$ share identical 3D surface plots and bottom projections, while Fig. 9(c) demonstrates that the pole $\mathrm{Re}[s_{\mathrm{p3}}]$ remains negative across the entire parameter range $-1.413\ \mathrm{V}<V<1.413\ \mathrm{V}$. The results indicate that the neuron is asymptotically stable over the voltage ranges $-1.395\ \mathrm{V}<V<-1.332\ \mathrm{V}$, $-0.824\ \mathrm{V}<V<0.824\ \mathrm{V}$, and $1.332\ \mathrm{V}<V<1.395\ \mathrm{V}$, where the real parts of all poles remain negative, i.e., $\mathrm{Re}[s_{\mathrm{p1,2,3}}]<0$.

Figure 9(d) presents the parameter map of the third-order neuron in the ω vs. V plane. The overlap between the red and gray regions corresponds to the EOCD, where the neuron is locally active and stable, over the voltage ranges $-1.395\ \mathrm{V}<V<-1.332\ \mathrm{V}$, $-0.824\ \mathrm{V}<V<-0.629\ \mathrm{V}$, $0.629\ \mathrm{V}<V<0.824\ \mathrm{V}$, and $1.332\ \mathrm{V}<V<1.395\ \mathrm{V}$. The overlap between the dark-red and light-blue regions defines the RHP pole domain, where the neuron is locally active and unstable, and action potentials can be observed over the voltage ranges $-1.413\ \mathrm{V}<V<-1.395\ \mathrm{V}$, $-1.332\ \mathrm{V}<V<-0.824\ \mathrm{V}$, $0.824\ \mathrm{V}<V<1.332\ \mathrm{V}$, and $1.395\ \mathrm{V}<V<1.413\ \mathrm{V}$. The blue region corresponds to the locally passive domain (LPD), over the voltage ranges $V<-1.413\ \mathrm{V}$, $-0.629\ \mathrm{V}<V<0.629\ \mathrm{V}$, and $V>1.413\ \mathrm{V}$, within which no periodic spiking occurs. All figures are symmetric with respect to the voltage axis $V=0$ and frequency axis $\omega=0$.

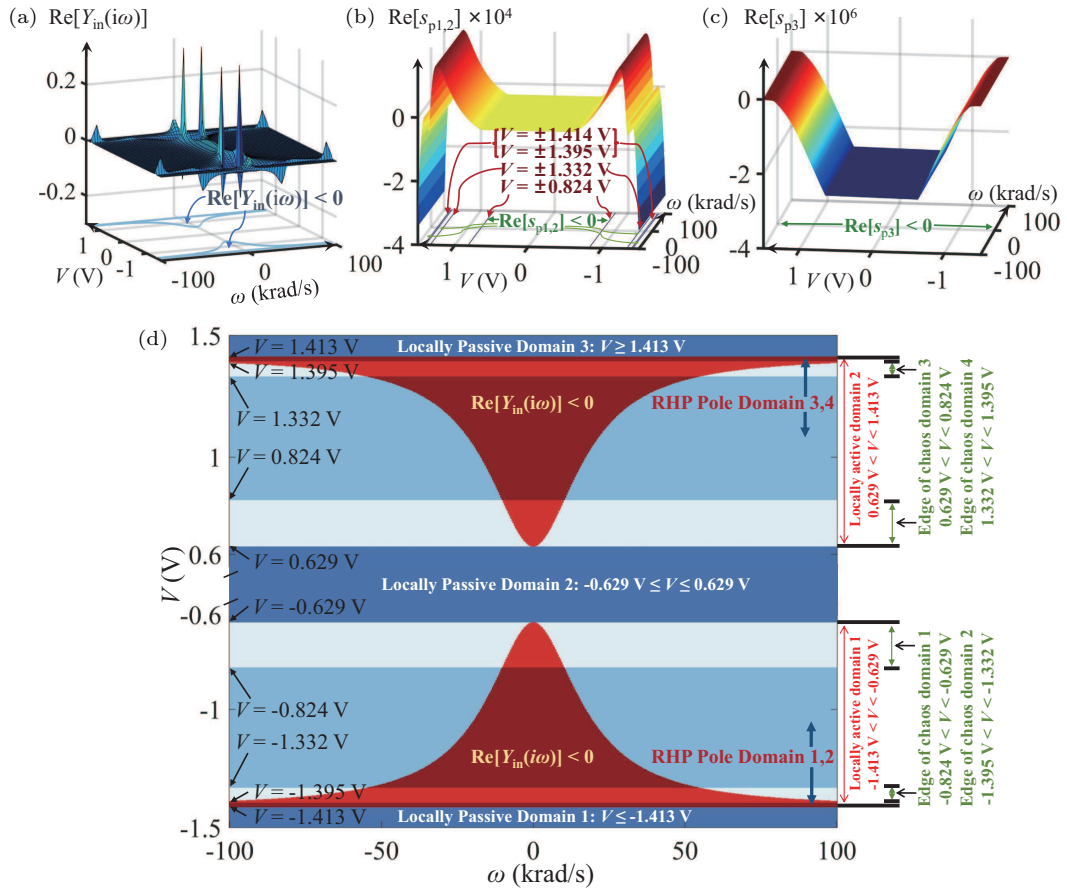


Fig. 9. (a) 3D surface plot of $\mathrm{Re}[Y_{\mathrm{in}}(\mathrm{i}\omega)]$ over the ranges $-100\ \mathrm{krad/s}<\omega<100\ \mathrm{krad/s}$ and $-1.5\ \mathrm{V}<V<1.5\ \mathrm{V}$. The bottom ω vs. V plane shows the sky-blue projection curve corresponding to $\mathrm{Re}[Y_{\mathrm{in}}(\mathrm{i}\omega)]=0$. (b) and (c) 3D surface plots of $\mathrm{Re}[s_{\mathrm{p1,2}}]$ and $\mathrm{Re}[s_{\mathrm{p3}}]$ over the ranges $-100\ \mathrm{krad/s}<\omega<100\ \mathrm{krad/s}$ and $-1.5\ \mathrm{V}<V<1.5\ \mathrm{V}$. The projected lines at the bottom denote $\mathrm{Re}[s_{\mathrm{p1}}]=0$ and $\mathrm{Re}[s_{\mathrm{p2}}]=0$, which separate the unstable region ($\mathrm{Re}[s_{\mathrm{p1,2}}]>0$) from the stable region ($\mathrm{Re}[s_{\mathrm{p1,2}}]<0$). (d) Parameter map of the third-order neuron in the ω vs. V plane. The projected curves from (a) to (c) clearly distinguish the LAD, LPD, and EOCD regions. The EOCD corresponds to the overlap between the red and gray areas over the voltage ranges $-1.395\ \mathrm{V}<V<-1.332\ \mathrm{V}$, $-0.824\ \mathrm{V}<V<-0.629\ \mathrm{V}$, $0.629\ \mathrm{V}<V<0.824\ \mathrm{V}$, and $1.332\ \mathrm{V}<V<1.395\ \mathrm{V}$. The RHP pole domain is given by the intersection of the light-blue and dark-red areas over the ranges $-1.413\ \mathrm{V}<V<-1.395\ \mathrm{V}$, $-1.332\ \mathrm{V}<V<-0.824\ \mathrm{V}$, $0.824\ \mathrm{V}<V<1.332\ \mathrm{V}$, and $1.395\ \mathrm{V}<V<1.413\ \mathrm{V}$.

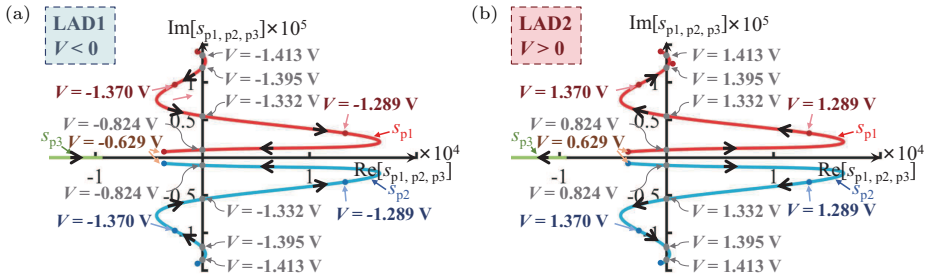


Fig. 10. Migration trajectories of the poles of the third-order neuron with inductor $L = 5.4$ mH and capacitor $C = 10$ nF in LAD1 over the voltage range $-1.413\ \text{V} < V < -0.629\ \text{V}$ in panel (a) and in LAD2 over the voltage range $0.629\ \text{V} < V < 1.413\ \text{V}$ in panel (b).

Additionally, the migration trajectories of the poles s_{p1}, s_{p2}, and s_{p3}, defined by Eq. (15), over the ranges $-1.413\ \text{V} < V < -0.629\ \text{V}$ and $0.629\ \text{V} < V < 1.413\ \text{V}$ are plotted in Fig. 10 to further examine the oscillation mechanism of the action potentials of the third-order neuron.

Figure 10 illustrates the migration trajectories of the poles s_{p1}, s_{p2}, and s_{p3} of the third-order neuron over the ranges $-1.413\ \text{V} < V < -0.629\ \text{V}$ and $0.629\ \text{V} < V < 1.413\ \text{V}$, with black arrows indicating the migration directions of the poles as the voltage V rises. Note that the arrows in Figs. 10(a) and 10(b) point in opposite directions, while the pole s_{p3} remains negative real. As shown in Fig. 10(a), the complex conjugate poles s_{p1} and s_{p2} in LAD1 originate near the negative real axis at $V = -1.413$ V and move toward each other as V increases. They bend toward the imaginary axis and successively pass four Hopf bifurcation points at $V = -1.413$ V, $V = -1.395$ V, $V = -1.332$ V, and $V = -0.824$ V. When the poles move into the right-half plane, i.e., $\text{Re}[s_{\text{p1,2}}] > 0$, the neuron becomes unstable and action potentials emerge, revealing the onset of chaos in the third-order neuron. Ultimately, the poles s_{p1} and s_{p2} terminate at $V = -0.629$ V.

Compared with the pole migration for negative voltages in LAD1 displayed in Fig. 10(a), Fig. 10(b) presents the reversed motion over the range $0.629\ \text{V} < V < 1.413\ \text{V}$ in LAD2. Collectively, the third-order neuron exhibits the same destabilization as the second-order neuron within its two symmetric LADs as a function of the input voltage $v_{\text{in}} = V$, enabling bidirectional spiking under both positive and negative inputs.

4.2. Frequency-tunable spiking

Based on Eq. (12), the output voltage $v_{\text{out}}(t)$ of the neuron is obtained, and its time-domain waveforms under different input voltages are presented in Fig. 11.

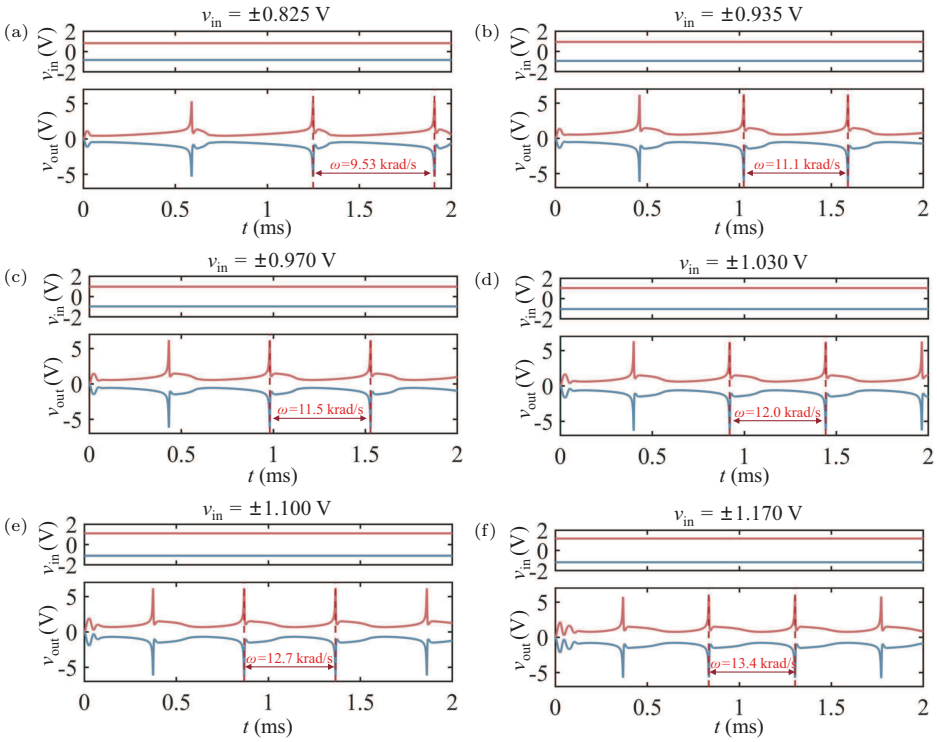


Fig. 11. Time-domain waveforms of the output voltage $v_{\text{out}}(t)$ at different frequencies of the third-order neuron for input voltages: $v_{\text{in}} = \pm 0.825$ V in panel (a), $v_{\text{in}} = \pm 0.935$ V in panel (b), $v_{\text{in}} = \pm 0.970$ V in panel (c), $v_{\text{in}} = \pm 1.030$ V in panel (d), $v_{\text{in}} = \pm 1.100$ V in panel (e), and $v_{\text{in}} = \pm 1.170$ V in panel (f), where the light-red spiking in the upward direction corresponds to a positive input voltage, while the steel-blue spiking in the opposite direction corresponds to a negative input voltage.

Figure 11 shows the output voltage waveforms $v_{\rm out}(t)$ of the third-order neuron in Fig. 8 under different input voltages $v_{\rm in}$. In each figure, the upper panels illustrate the positive (light-red) and negative (steel-blue) input voltages $v_{\rm in}$, while the lower panels show the associated output waveforms. As $v_{\rm in} = \pm 0.825$ V, the neuron generates periodic spiking at $\omega = 9.53$ krad/s, marked by the two red dotted lines, upward for positive input and inverted for negative input, as shown in Fig. 11(a). With progressively larger input voltages $v_{\rm in}$, the neuron generates sustained periodic spiking, and the corresponding oscillation frequency increases monotonically, demonstrating a positive relationship between frequency and voltage, as shown in Figs. 11(b)–11(f).

Figure 11 reveals a monotonic increase in spiking frequency ω with increasing input voltage $v_{\rm in}$, thereby demonstrating the frequency-tunable spiking dynamics in the OS-CCM-based third-order neuron.

4.3. Quantitative analysis of frequency characteristics

To quantitatively analyze the frequency characteristics of the output spiking, the loci of the measured frequency ω of the output spiking and the imaginary part values of the poles $\mathrm{Im}[s_{\rm p1,2}]$ of the third-order neuron in Fig. 8 under different input voltages $v_{\rm in} = V$ are plotted in Fig. 12.

Figure 12 shows the loci of the measured frequency ω of the output spiking at $v_{\rm in} = V$ and the imaginary parts of the pair of complex-conjugate poles $\mathrm{Im}[s_{\rm p1,2}]$ of the neuron at the corresponding operating point Q^* with $V_{\rm C} = V_{\rm M} = V$. Figure 12(a) indicates that the measured frequency ω (black) closely matches the imaginary part of the pole $\mathrm{Im}[s_{\rm p1}]$ and the absolute value of $\mathrm{Im}[s_{\rm p2}]$ (green), where $\mathrm{Im}[s_{\rm p2}] = -\mathrm{Im}[s_{\rm p1}]$, with a mean error less than 4% for input voltages over the range $-1.100\ \mathrm{V} < V < -0.820\ \mathrm{V}$. Note that the third-order neuron has only three poles, including one real negative pole and one complex-conjugate pair. Likewise, Fig. 12(b) illustrates the same conclusion for input voltages over the range $0.820\ \mathrm{V} < V < 1.100\ \mathrm{V}$. Consistent with the second-order case, the third-order neuron maintains frequency controllability and predictability. The approximate relation $\omega = |\mathrm{Im}[s_{\rm p1,2}]|$ can be established. Moreover, the magnitude of the voltage-dependent frequency modulation is noticeably stronger, demonstrating enhanced tunability inherent in the higher-order neuron.

This section demonstrates that the third-order neuron possesses frequency-tuning capability and that its spiking frequency is directly determined by the imaginary part of the poles, confirming that pole locations reliably predict the oscillation frequency. In contrast to the second-order case, the third-order neuron exhibits a more distinct and enhanced voltage-frequency relationship, providing further evidence of the universality of this tuning mechanism across OS-CCM-based neuronal circuits.

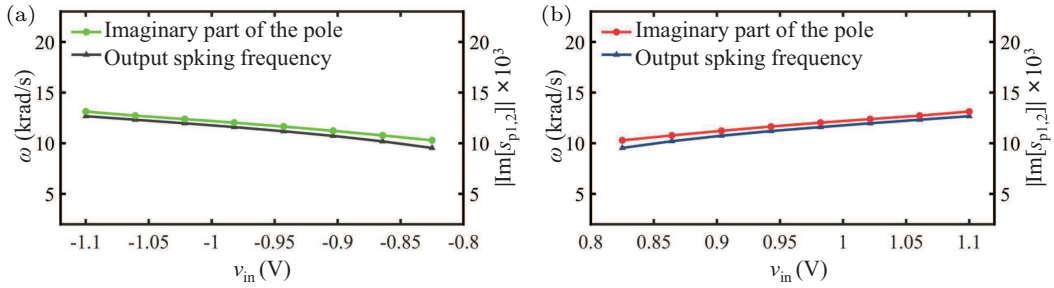


Fig. 12. Loci of the measured frequency ω of the output spiking of the neuron in Fig. 8, and the imaginary part of its poles $\mathrm{Im}[s_{\rm p1,2}]$ over the ranges $-1.100\ \mathrm{V} < V < -0.820\ \mathrm{V}$ in panel (a) and $0.820\ \mathrm{V} < V < 1.100\ \mathrm{V}$ in panel (b) within the RHP pole domain.

5. Hardware verification of the frequency-tunable spiking

A functional physical OS-CCM circuit made of off-the-shelf electronic components has been built in our work,[21] whose circuit schematic is reproduced in Fig. 13(b) for the reader's convenience. The second- and third-order neuron hardware circuits can be implemented using this physical OS-CCM circuit board together with an external inductor and a capacitor, whose circuit schematics are displayed in Figs. 13(a) and 13(c).

Figures 13(a) and 13(c) show the second- and third-order neuron circuits, in which the memristor is built from off-the-shelf discrete components, including four op-amps (TL082CP and TL084CN), three multipliers (AD633JNZ), several resistors, and a capacitor, as shown in Fig. 13(b). The voltages VCC = 15 V, VEE = −15 V, VSS = −7.81 V, and VDD = 7.81 V provide power for the op-amps and multipliers embedded in the memristor hardware circuit boards.

Integrating an OS-CCM hardware circuit with an inductor of 5.4 mH yields the second-order neuron hardware circuit board. As the input voltages of the neuron lie over the ranges $-1.139\ \mathrm{V} < V < -0.956\ \mathrm{V}$ and $0.956\ \mathrm{V} < V < 1.139\ \mathrm{V}$ in its RHP pole sub-domains, the measured spiking frequency of the second-order neuron can be observed in Fig. 14.

Figure 14 shows the measured output voltage waveforms $v_{\rm out}(t)$ of the second-order neuron hardware circuit board in Fig. 13(a) under different input voltages $v_{\rm in}$. As $v_{\rm in} = 0.956$ V (resp. $v_{\rm in} = -0.956$ V), the neuron generates periodic spiking at a frequency of $\omega = 10.00$ krad/s, marked by the two white dotted lines, upward for positive input (resp. downward

for negative input), as shown in Fig. 14(a). The corresponding theoretical frequency is 11.2 krad/s, resulting in a percentage error of approximately 11%. Increasing the magnitude of the input voltage $v_{\rm in}$ leads to a higher spike frequency, as observed in Figs. 14(b)–14(d), which verifies the theoretical prediction that the OS-CCM-based second-order neuron exhibits frequency-tunable action potentials. The slight phase mismatch between forward and reverse periodic spiking arises from measurement instrument errors and non-idealities of the hardware circuit boards.

By adding a 10 nF capacitor to the second-order neuron physical circuit, the third-order neuron hardware circuit board is obtained. For input voltages within the RHP pole sub-domain ranges $-1.170\ {\rm V} < V < -0.970\ {\rm V}$ and $0.970\ {\rm V} < V < 1.170\ {\rm V}$, the measured action potentials of the third-order neuron are shown in Fig. 15.

Figure 15 presents the experimentally measured output voltage waveforms $v_{\rm out}(t)$ of the third-order neuron in Fig. 13(c) under different input voltages $v_{\rm in}$. Yellow upward spiking corresponds to positive input, whereas cyan downward spiking corresponds to negative input. As shown in Fig. 15(a), the neuron exhibits periodic spiking at a frequency of $\omega = 9.69$ krad/s for $v_{\rm in} = \pm 0.970$ V. The corresponding theoretical frequency in Section 4 is 11.5 krad/s, giving a percentage error of approximately 16%. Figures 15(b)–15(d) show that the spiking frequency increases monotonically with input voltage, confirming the frequency-tunable behavior of the OS-CCM-based third-order neuron.

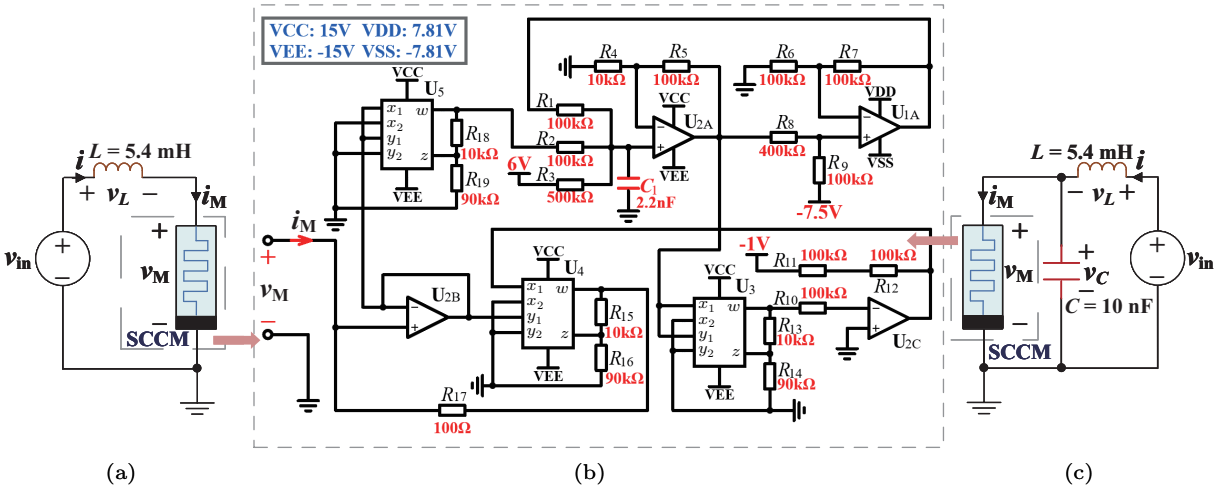


Fig. 13. (a) Circuit schematic of the second-order neuron circuit composed of a physical OS-CCM circuit and an inductor. (b) Circuit schematic implementing the OS-CCM defined by Eqs. (1) and (2). (c) Circuit schematic of the third-order neuron circuit composed of a physical OS-CCM circuit, an inductor, and a capacitor.

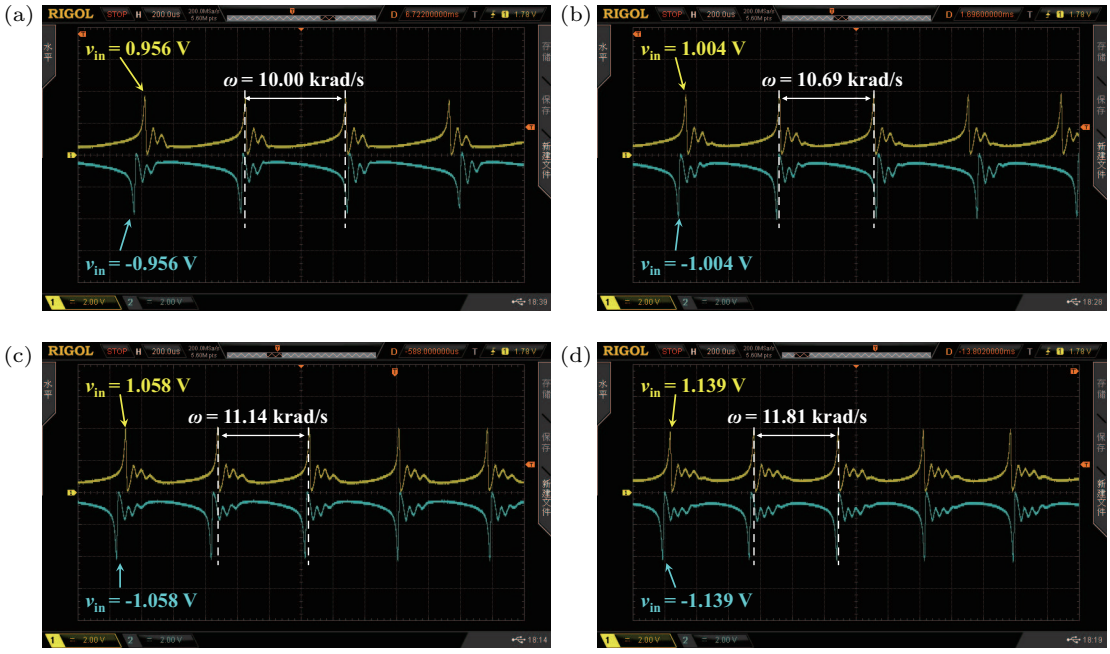


Fig. 14. Measured output voltage waveforms $v_{\rm out}(t)$ of the second-order neuron at different input voltages: $v_{\rm in} = \pm 0.956$ V in panel (a), $v_{\rm in} = \pm 1.004$ V in panel (b), $v_{\rm in} = \pm 1.058$ V in panel (c), and $v_{\rm in} = \pm 1.139$ V in panel (d). The yellow action potentials in the upward direction correspond to a positive input voltage, while the cyan action potentials in the downward direction correspond to a negative input voltage.

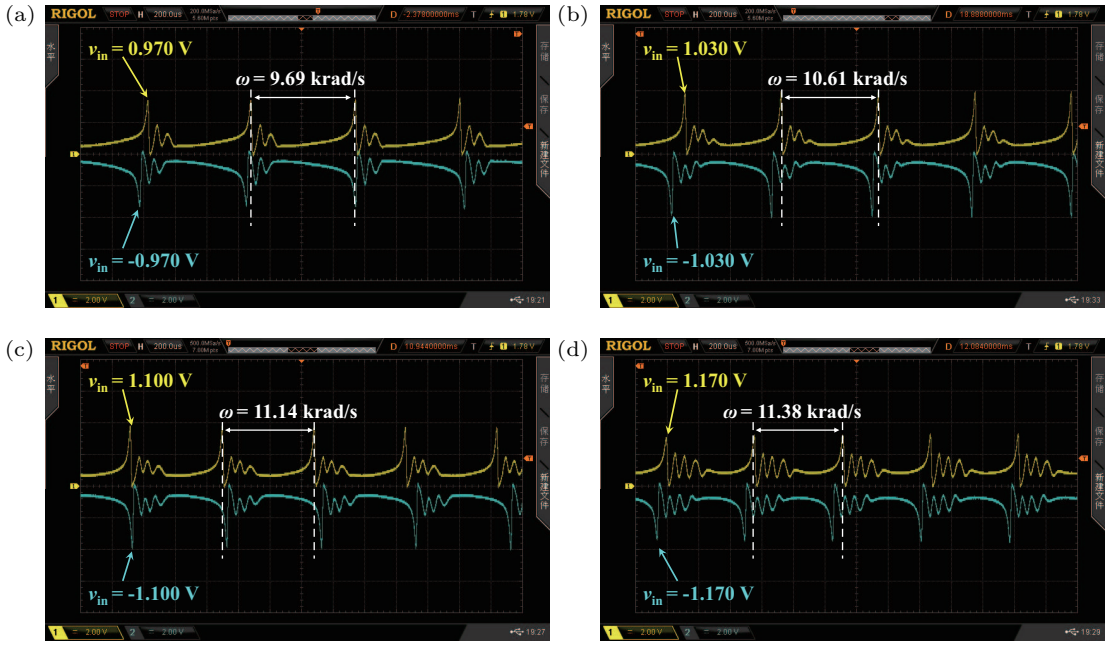


Fig. 15. Measured output voltage waveforms $v_{out}(t)$ of the third-order neuron at different input voltages: $v_{in} = \pm 0.970$ V in panel (a), $v_{in} = \pm 1.030$ V in panel (b), $v_{in} = \pm 1.100$ V in panel (c), and $v_{in} = \pm 1.170$ V in panel (d). The yellow action potentials in the upward direction correspond to a positive input voltage, while the cyan action potentials in the downward direction correspond to a negative input voltage.

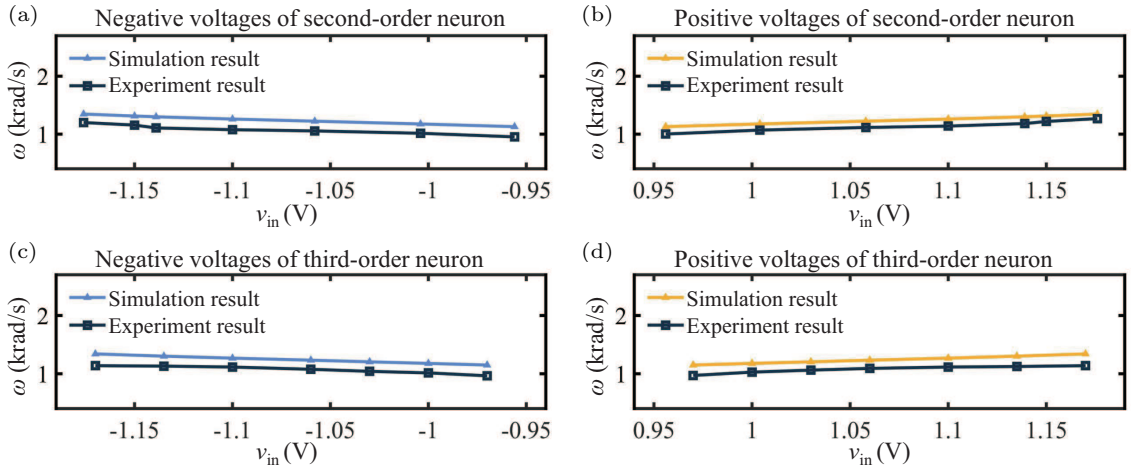


Fig. 16. Trajectories of the output frequency ω for both simulation and experimental results. Simulation results are shown in blue and yellow, while experimental measurements are shown in black. Panels (a) and (b) correspond to the second-order neuron over the negative and positive input voltage ranges -1.176 V $< V < -0.956$ V and 0.956 V $< V < 1.176$ V, respectively. Panels (c) and (d) correspond to the third-order neuron over the negative and positive input voltage ranges -1.170 V $< V < 0.970$ V and 0.970 V $< V < 1.170$ V, respectively.

To further compare the spiking frequency of the neuron circuits in Figs. 3(b) and 8 with the experimentally measured frequencies in Fig. 13, the frequency trajectories of simulation and experimental results under different input voltages $v_{in} = V$ are plotted in Fig. 16.

Figure 16 shows the trajectories of the measured frequency ω for simulation results (yellow) obtained in the second- and third-order neuron circuits in Figs. 3(b) and 8, and for experimental results (black) measured in the corresponding hardware circuits in Fig. 13. The close agreement between experimental and theoretical results indicates strong consistency between theory and practice for the OS-CCM-based neurons.

A programmable laboratory power supply delivers tunable dual-polarity voltage inputs, while the DC–DC conversion board provides stable operating voltages for all analog elements on the neuron boards. The experimental setup is shown in Fig. 17.

Figure 17 shows the experimental setup, including two printed circuit boards of OS-CCM-based neurons to produce upward and opposite spiking, along with measurement instruments such as an oscilloscope, power supply, and digital multimeter. Two identical neuron circuit boards, with positive and negative input voltages applied simultaneously, generate symmetric output voltages, which are monitored on the oscilloscope on the right. A DC–DC circuit board with a voltage resolution of 0.001 V supplies power to the analog components.

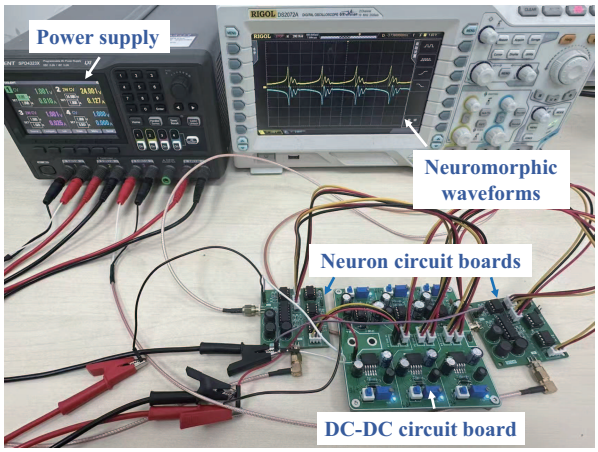


Fig. 17. Experimental setup showing two printed circuit boards of OS-CCM-based neurons under positive and negative input voltages, along with the associated measurement instruments.

This section provides hardware verification of the frequency-tunable action potentials of the second- and third-order neuron circuits based on the OS-CCM physical circuit board, confirming that the theoretically predicted frequencies closely match the experimentally measured spiking frequencies. These results substantiate the reliability of the proposed memristive neuron.

6. Conclusion

This paper employed a CCM variant, the OS-CCM, to demonstrate frequency-tunable spiking in second- and third-order memristive neurons. The spiking frequency of the neurons increased with the amplitude of the external stimulating voltage. Theoretical analysis indicated that the measured spiking frequency of the neurons closely approximates the imaginary part of the poles of the small-signal admittance function at the operating point. Thus, the imaginary part of the poles can be used to predict the output spiking frequency.

Second- and third-order neuron hardware circuits were constructed using a homemade OS-CCM physical circuit board. Both simulation and experimental results verified the theoretical analysis. The frequency-tunable spiking dynamics investigated in this study could be applied to information encoding and transmission in brain-inspired computing. Overall, this work establishes a general and physically interpretable framework for analyzing and predicting spiking-frequency dynamics in memristive neurons, providing theoretical support for frequency-programmable neuromorphic systems.

Acknowledgments

This project was supported by the National Natural Science Foundation of China (Grant Nos. 62501213, 62574072, 62571172, and 62301202), the Zhejiang Provincial Natural Science Foundation of China (Grant Nos. LQN25F010008 and LQ24F010015), the Fundamental Research Funds for the Provincial Universities of Zhejiang (Grant No. GK249909299001-025), and the National College Students Innovation and Entrepreneurship Training Program of China (Grant No. 202410336019).

References

[1] Sun J W, Shen Y J, Wang Y C and Wang Y F 2025 *IEEE Trans. Neural Netw. Learning Syst.* **36** 11466
[2] Sun J W, Gao P L, Liu P and Wang Y F 2025 *IEEE Trans. Ind. Inf.* **21** 5633
[3] Wang Y F, Tao K F, Wang Z C and Sun J W 2025 *IEEE Trans. Ind. Inf.* **21** 5777
[4] Huo Q, Yang Y M, Wang Y M, Lei D Y, Fu X Q, Ren Q R, Xu X X, Luo Q, Xing G Z, Chen C Y, Si X, Wu H, Yuan Y Y, Li Q, Li X R, Wang X H, Chang M F, Zhang F and Liu M 2022 *Nat. Electron.***5** 469
[5] Li X S, Sun J R, Sun Y C and Zhang J L 2025 *IEEE Trans. Circuits Syst. I* **72** 8028
[6] Sun J R, Sun J W, Li X S, Sun Y C, Hong Q H and Wang C H 2025 *Nonlinear Dyn.* **113** 33035
[7] Sun J R, Li X S, Sun Y C, Xiong Z N and He J Q 2026 *Chin. Phys. B* **35** 010501
[8] Chen Q X, Lu L, Meng J L, Xu M S and Wang T Y 2025 *Research* **8** 0916
[9] Hussein S Y S H and Ho P W C 2025 *Eng. Res. Express* **7** 032201
[10] Weiher M, Herzig M, Telzlaff R, Ascoli A, Mikolajick T and Slesazeck S 2019 *IEEE Trans. Circuits Syst. I* **66** 2627
[11] Ying J J, Liang Y, Li F P, Wang G Y and Shen Y R 2022 *Electronics* **11** 665
[12] Chua L, Sbitnev V and Kim H 2012 *Int. J. Bifurcation Chaos* **22** 1230011
[13] Yi W, Tsang K K, Lam S K, Bai X, Crowell J A and Flores E A 2018 *Nat. Commun.* **9** 4661
[14] Kumar S, Williams R S and Wang Z 2020 *Nature* **585** 518
[15] Zhu J X, Zhang X M, Wang R, Wang M, Chen P, Cheng L L, Wu Z H, Wang Y Z, Liu Q and Liu M 2022 *Adv. Mater.* **34** 2200481
[16] Yuan F, Li S Y, Deng Y, Li Y X and Chen G R 2023 *IEEE Trans. Ind. Electron.* **70** 4120
[17] Yuan F, Yu X C, Deng Y, Li Y X and Chen G R 2024 *IEEE Trans. Ind. Electron.* **71** 9480
[18] Jin P P, Wang G Y, Liang Y, Lu H HC and Chua L O 2021 *IEEE Trans. Circuits Syst. I* **68** 4419
[19] Jin P P, Wang G Y, Liang Y, Chen L, Iu H H and Chua L 2023 *IEEE Trans. Circuits Syst. II* **70** 3139
[20] Chua L 2023 *IEEE Electron Devices Mag.* **1** 10
[21] Jin P P, Wang G Y and Chen L 2023 *Chaos* **33** 023120
[22] Jin P P, Ascoli A, Wang G Y, Liang Y, Wang X W, Yuan F, Dong Y J, Chen L, Iu H H, Demirkol A S, Tetzlaff R and Chua L 2025 *IEEE Trans. Circuits Syst. I* **73** 2015
[23] Li H D and Min F H 2025 *IEEE Trans. Circuits Syst. I* **72** 4820
[24] Li H D and Min F H 2025 *IEEE Internet Things J.* **12** 29018
[25] Ying J J, Min F H and Wang G Y 2023 *Chaos Solitons & Fractals* **175** 114058
[26] Liu D H, Wang K H, Cao Y H and Lu J S 2024 *Electronics* **13** 2776
[27] Xu Q, Wang K, Chen M, Parastesh F and Wang N 2024 *Chaos, Solitons & Fractals* **181** 114654
[28] Hua Z Y, Chen Y Y, Bao H and Zhou Y C 2022 *IEEE Trans. Syst. Man Cybern, Syst.* **52** 4402
[29] Zhang Y X, Hua Z Y, Bao H and Huang H J 2024 *IEEE Trans. Circuits Syst. I* **71** 2783
[30] Yang Y, Zhu F D, Zhang X M, Chen P, Wang Y Z, Zhu J X, Ding Y T, Cheng L L, Li C, Jiang H, Wang Z R, Lin P, Shi T, Wang M, Liu Q, Xu N S and Liu M 2024 *Nat. Commun.* **15** 4318
[31] Li J D, Zhao W, Fu C W, Zhai Z P, Xu P F, Diao X Y, Guo W L and Yin J 2025 *Nat. Commun.* **16** 7911
[32] Chua L 2005 *Int. J. Bifurcation Chaos* **15** 3435
[33] Mannan Z I, Choi H and Kim H 2016 *Int. J. Bifurcation Chaos* **26** 1630009